



Vacuum-free arc synthesis and characterization of crystalline molybdenum borides as instrumental material

Yuliya Vassilyeva ^{a,*}, Yulia Neklyu ^a, Mikhail Lukonov ^b, Alexander Kvashnin ^b, Alexander Pak ^a

^a National Research Tomsk Polytechnic University, 30 Lenin Avenue, Tomsk 634050, Russia

^b Skolkovo Institute of Science and Technology, Skolkovo Innovation Center, Bolshoy Boulevard 30, bld. 1, Moscow 121205, Russia



ARTICLE INFO

Keywords:
Molybdenum boride
Higher boride
Arc discharge
Vacuum-free method
Electric arc reactor
Open-air environment

ABSTRACT

Transition metal borides are a fascinating class of materials that have garnered significant attention in various fields due to their unique properties and diverse applications. Here the possibility of obtaining crystalline phases in the molybdenum-boron system by direct current (DC) arc discharge method under ambient air conditions is presented for the first time. The synthesis process can be carried out in an open-air environment, which significantly simplifies the design of electric arc reactors and increases the efficiency of desired materials. The influence of different parameters, such as the power supply current, arc exposure time, the Mo:B ratio in the raw powder material on the phase composition of the synthesis products is studied. As a result, almost all known phases of molybdenum borides, namely $I4/mcm$ -Mo₂B, $I4_1/amd$ -MoB (α -MoB), $Cmcm$ -MoB (β -MoB), $P1$ -Mo₂B₁₁, $R\bar{3}m$ -MoB₂, $P6_3/mmc$ -MoB₃, as well as practically unexplored higher boride $P6_3/mmc$ -MoB_{5-x} are synthesized. Convolution neural network (CNN) trained on the computational data of known molybdenum borides allows the analysis of experimental X-ray diffraction data and identification of individual phases in the synthesized powders. The optimal parameters of synthesis are determined to obtain samples with ~70 wt% of higher molybdenum boride MoB_{5-x}: current strength of 200 A, arc exposure time of 40 s, molybdenum to boron atomic ratio of 1:17. Synthesized powder is then used to sinter ceramic samples to measure the mechanical properties, such as hardness and elastic modulus. The findings of this study are much more extensive than those presented here. They offer a potential for rapid and cheap synthesis of instrumental materials based on molybdenum borides, which possess high mechanical properties.

1. Introduction

Transition metal borides are a fascinating class of materials that have garnered significant attention in various fields due to their unique properties and diverse applications. In the field of materials science, they are often utilized as hard coatings and cutting tools due to their superior wear resistance. Boron-based materials attract attention due to their physical and chemical properties, such as unique structural complexity, high mechanical strength, superconductivity, thermoelectric properties, excellent chemical stability, and high catalytic performance [1]. They have wide applications as efficient catalysts, thermal neutron detectors, and are used in flat-panel displays and electron emission nanodevices [2–4]. The Mo-B phase diagram includes a big variety of phases: Mo₂B, MoB, MoB₂, Mo₂B₅ и Mo_{1-x}B₃ (MoB₄) [5]. The molybdenum-boron system compounds have potential for

constructional and instrumental applications requiring heat resistance due to their high melting point (2600, 2375 and 2140 °C for MoB, MoB₂ and Mo₂B₅, respectively), chemical stability, corrosion resistance, high hardness and strength [6]. Also, the properties of molybdenum borides allow considering them for potential applications in wear-resistant or corrosion-resistant coatings, ceramic composites, synthesis of other compounds and as electrocatalysts for hydrogen evolution reaction [7].

Despite the fact that the study of Mo-B compounds began in 1940, there are still ongoing studies indicating the possibility of the existence of new crystalline phases of higher borides. Studies of the molybdenum-boron system by using computational methods, including those using the USPEX evolutionary algorithm [8,9], indicate the presence of stable ($I4_1/amd$ -MoB (α -MoB), $R\bar{3}m$ -MoB₂ и Pmmn-MoB₅) and metastable ($I4/mcm$ -Mo₂B, $P4/mbm$ -Mo₃B₂, $Cmcm$ -MoB (β -MoB), $P6_3/mmc$ -MoB₂,

* Corresponding author.

E-mail address: yv1@tpu.ru (Y. Vassilyeva).

$P6/mmm$ -MoB₂, $P6_3/mmc$ -Mo₂B₅, $R3\bar{m}$ -MoB₃ и $P6_3/mmc$ -MoB₄) phases.

To date, several methods for the synthesis of molybdenum borides have been proposed: chemical vapor deposition – CVD [4], used to produce pure ultrathin films at high temperatures (900 °C); mechanochemical method [10], realized by long-term grinding of the initial components in an argon atmosphere followed by pressing and annealing; self-propagating high-temperature synthesis – SHS [11,12], which is based on exothermic reactions to obtain crystalline phases of molybdenum boride; hydrothermal synthesis [13], producing nanoscale molybdenum boride at a relatively low temperature (300 °C) in an autoclave; arc melting method [14], in which the initial powders are pressed and melted in an arc furnace in an argon atmosphere with repeated remelting; HPHT method [15] for obtaining sintered samples of molybdenum boride under high pressure and temperature; synthesis with volumetric combustion [4], implemented in a similar way to SHS. Regarding the crystalline phases of molybdenum borides and their synthesis methods, the molten salt method was used to obtain molybdenum monoborides (α -MoB) and molybdenum diborides (MoB₂ and Mo₂B₄) using Mo-Cl₅ and elemental boron in the presence of the metal precursor Sn [16]. The authors obtained the crystalline phases Mo₂B, α -MoB, β -MoB and α -MoB₂ by arc melting [14]. The Mo₃B thin film was obtained by CVD using a mixture of boron powders and boron oxide [4]. The crystalline phases Mo₂B, MoB, α -MoB₂ and β -MoB₂ can be synthesized by sintering at high temperature (1600–1800 °C) and pressure (5.2 GPa) [17]. In addition, it is reported that the highest phase of molybdenum boride (called MoB₄, Mo_{1-x}B₃ or MoB₃) was obtained at high pressure (15 GPa) and high temperature (1650–1750 °C) [18]. However, experimental studies on obtaining and studying the properties of higher molybdenum borides are almost absent. Accordingly, the development of efficient methods to synthesize molybdenum borides, including higher borides, appears to be a pressing task.

Recently, higher tungsten boride WB_{5-x} (as well as other tungsten borides), a structural analog of higher molybdenum boride, was obtained by electric arc synthesis method in an open-air environment [19]. This fact suggests the possibility of synthesizing molybdenum borides, including higher borides, by the above method. The advantage of the vacuum-free electric arc method is the realization of arcing at normal pressure under ambient conditions, which leads to a significant simplification of the electric arc reactor due to the absence of a sealed chamber and special equipment for creating special conditions of the gas environment, such as vacuum.

Here we present results of synthesis and characterization of crystalline molybdenum-boron compounds with different boron concentration by using the vacuum-free electric arc method. The composition of the obtained samples is investigated by the combination of X-ray diffraction analysis together with convolution neural network (CNN) trained on computational data. Data for interpretation is taken from the PDF4+ database and from results of computational prediction of crystal structures with evolutionary algorithm USPEX [20–22]. As a result, the possibility of obtaining a sample containing ~70 wt% of the higher molybdenum boride phase MoB_{5-x} under certain synthesis conditions (Mo:B = 1:17, 200 A, 40 s) is established. Moreover, ceramics based on synthesized powders are obtained by spark plasma sintering and their mechanical properties, such as hardness and elastic modulus, are investigated.

2. Materials and methods

2.1. Vacuum-free electric arc synthesis

The powders of nanoscale molybdenum (Advanced Powder Technologies LLC, Russia) and amorphous boron (Rare Metal, Russia) are mixed in a Retsch PM100 planetary ball mill for 15 min at 400 rpm in a WC grinding bowl (mass ratio of powder and grinding balls was 1:15) and used as an initial mixture. SEM-images and elemental mapping of

initial components are shown in Fig. S1 in the Supporting Information.

The studies are carried out on the original electric arc reactor, the simplified scheme is shown in Fig. 1a. Electrodes are connected to the DC power supply: anode is a graphite rod of round cross-section with a diameter of 8 mm and a length of 100 mm, cathode – a small graphite crucible with an outer diameter of 20 mm and a height of 20 mm, covered with a graphite lid. A small graphite crucible are placed in a graphite crucible of large dimensions (outer diameter 40 mm, height 40 mm) in order to keep the autonomous gas environment, which is formed by the influence of carbon plasma and air with the formation of CO and CO₂ gases [19], as well as to improve the thermal insulation characteristics of the enclosing structure of the reaction zone. To estimate the consumption of graphite electrodes in the process of vacuum-free electric arc synthesis, an analysis of the mass balance of graphite elements (rod, small crucible, lid, large crucible) was performed (Fig. S2 in the Supporting Information). The DC arc discharge is initiated between the anode and the lid of the inner crucible, in which the initial mixture with a mass of 0.50 g ± 0.01 g are placed, as shown in Fig. 1a.

Several series of experiments are performed to obtain all known phases in the molybdenum-boron system using the vacuum-free electric arc method: in the first series varying the power supply current from 50 A to 200 A, plasma exposure time was 40 s, ratio Mo:B = 1:3 at; in the second series varying the plasma exposure time from 10 to 60 s at current 200 A and ratio Mo:B = 1:3 at; in the third series varying ratio of the initial components Mo:B with increase of boron fraction from 1 to 30 at. parts, current was 200 A, time of electric arc plasma treatment was 40 s. The parameters of experiments are shown in Table S2. A typical oscillogram obtained during an experiment are shown in Fig. S3 (in the Supporting Information).

Analysis of the gas medium composition during the synthesis of molybdenum borides is performed using a gas analyzer TEST 1 (Boner, Russia). The gas analyzer probe is inserted into the cavity of the external graphite crucible. The study of the temperature field in the process of DC arc discharge is carried out using an infrared camera PI 1 M (Optris, Germany). For this a separate experiment was conducted, in which a rectangular groove equal to the height of the inner (small) crucible was made in the wall of the outer graphite crucible. In this case, to exclude the possibility of damage to the matrix of the infrared camera by arc radiation, the area of arc discharge combustion was separated from the camera lens by a protective screen. The temperature was measured in the upper and lower parts of the outer crucible and the inner crucible filled with the initial mixture. Using the software of the infrared camera, the integral value for the area of the outer and inner crucibles was calculated.

2.2. Spark plasma sintering Mo-B ceramics

Consolidation of synthesized powders to obtain bulk ceramic samples by spark plasma sintering (SPS) was performed using GT Advanced Technologies SPS 10-4 (USA) in vacuum. The powder was poured into a graphite die of 12.7 mm inner diameter, and the die was placed between the graphite electrodes in an SPS chamber. The process of compaction was conducted in vacuum under the pressure of 50 MPa. The powders were sintered at 1650 °C with a heating rate of 100 °C/min for 10 min. Finally, the sintered cylindrical samples of 12.7 mm diameter and 3 mm height were produced.

2.3. Characterization of samples

The phase composition of as-synthesized and sintered samples was studied by X-ray diffractometry on the XRD-7000S diffractometer (Shimadzu, Japan) under CuKa-radiation with $\lambda = 1.54060 \text{ \AA}$ in the range of 10–90°. The morphology and elemental composition were studied by VEGA 3 SBU scanning electron microscopy with an Oxford Instruments X-Max 50 silicon drift EDS system (TESCAN, Czech Republic) at accelerating voltage of 20 kV in the low vacuum regime with back-scattered

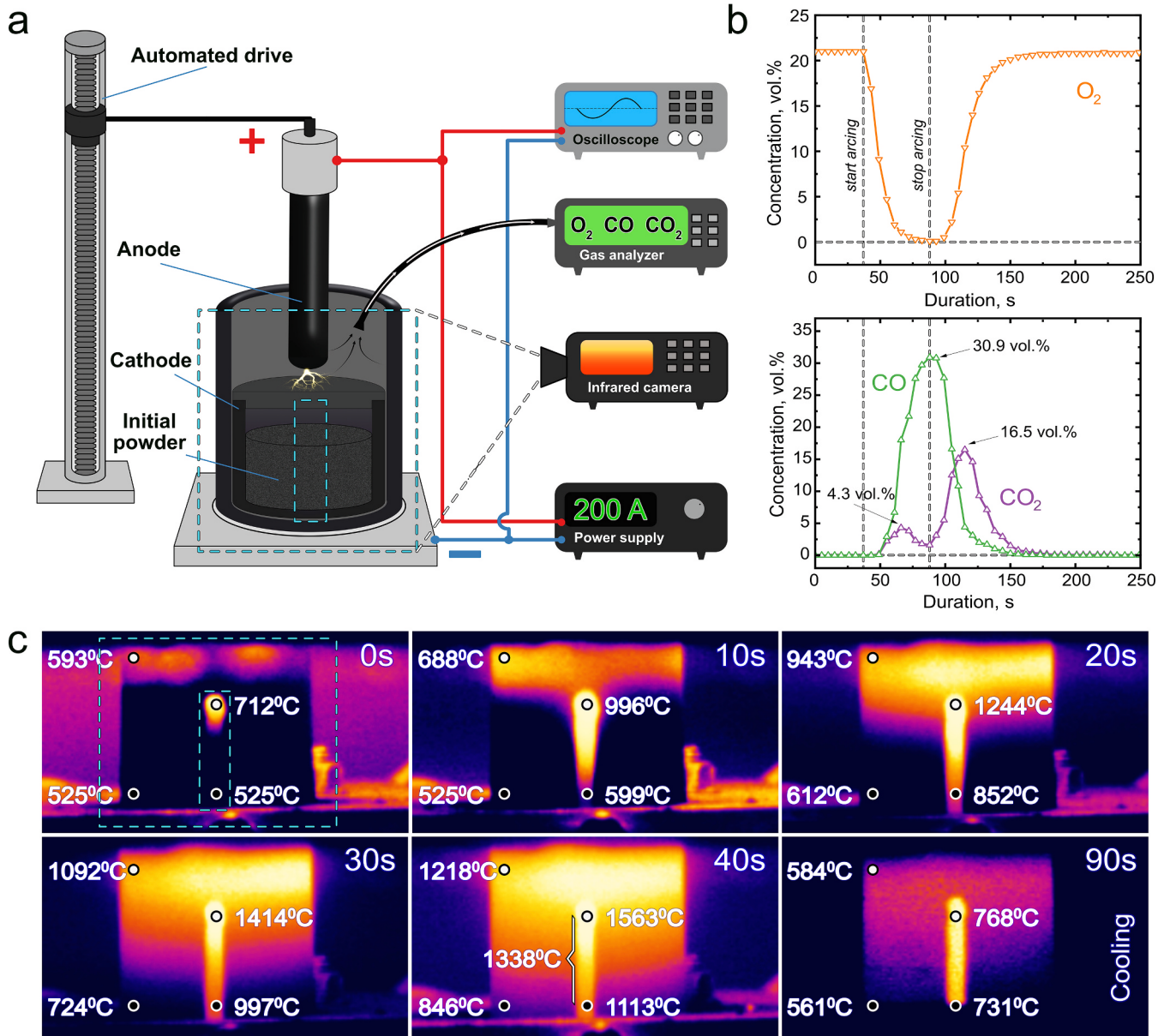


Fig. 1. Principal scheme of the vacuum-free DC arc discharge reactor (a); dependences of O_2 , CO and CO_2 concentrations recorded by gas analyzer during the synthesis (b); temperature field distribution during DC arcing (c).

electron and secondary electron detectors, and by transmission electron microscopy on the microscope JEM-2100 with an Oxford instrument EDS detector (JEOL, Japan) at accelerating voltage of 200 kV in the TEM, HRTEM, and STEM modes.

The relative density of sintered samples was determined by the Archimedes method using distilled water as a wetting liquid. The microstructure of the sintered materials was examined by SEM VEGA 3 SBU with an Oxford Instruments X-Max 50 silicon drift EDS system (TESCAN, Czech Republic). Measurements of elastic modulus value (Young's modulus E , shear modulus G) were derived from ultrasonic sound velocity measurements (Olympus 38 DL PLUS). The microhardness was measured in an indentation test using dynamic ultra-micro hardness tester DUH-211 (Shimadzu, Japan) with a Berkovich indenter. The applied load was equal to 100 . The average hardness was evaluated from at least 10 indentations made on each sample.

2.4. Crystal structure prediction and DFT calculations

The crystal structures of stable Mo-B structures are predicted using the first-principles variable-composition evolutionary algorithm search as implemented in the USPEX code [20–22]. During the structure search, the first generation of 160 structures was produced randomly with up to 32 atoms in the primitive unit cell. The succeeding generations were obtained by applying the heredity (40 %), softmutation (20 %), and transmutation (20 %) operators, respectively; 20 % of each generation is produced using the random symmetric [23].

Energy calculations during the evolutionary search are based on the density functional theory (DFT) [24,25] within the generalized gradient approximation (the Perdew–Burke–Ernzerhof functional) [26] and the projector augmented wave method [27,28] as implemented in the VASP [29–31] code. The plane wave energy cutoff of 400 eV, Methfessel–Paxton smearing [32] of electronic occupations, and Γ -centered k -point meshes with a resolution of $2\pi \times 0.025 \text{ \AA}^{-1}$ for the Brillouin zone sampling were used, ensuring convergence of the energy

differences and stress tensors.

The evolution of the convex hull phase diagram with temperature is obtained using the computed Gibbs free energies G of the relevant phases in the quasiharmonic approximation [33]:

$$G(P, T) = E_0(V) + F_{vib}(T, V) + P(T, V)V \quad (1)$$

where E_0 is the total energy from the DFT calculations and F_{vib} the vibrational Helmholtz free energy calculated as:

$$F_{vib}(T, V) = k_B T \int_{\Omega} g(\omega(V)) \ln \left[1 - \exp \left(-\frac{\hbar \omega(V)}{k_B T} \right) \right] d\omega + \frac{1}{2} \int g(\omega(V)) \hbar \omega d\omega \quad (2)$$

and pressure is

$$P(T, V) = -\frac{\partial(E_0(V) + F_{vib}(T, V))}{\partial V} \quad (3)$$

Here $g(\omega(V))$ is the phonon density of states at the given volume, calculated using the finite-displacement method using a combination of VASP [29–31] and PHONOPY. Once Gibbs free energies are computed, phase equilibrium lines on the phase diagram are determined as loci of points where free energies of phases are equal.

2.5. Crystal structure identification using neural networks

To make peak identification of the X-ray diffraction patterns and to determine the weight fraction of each phase a convolution neural network (CNN) is used which is based on the approaches proposed by Szymanski et al. [34]. The main problem of peak identification consists in general of some aspects: we need to have reference XRD patterns of the presumed phases, obtained experimentally or based on computer modelling and we need to make a valid comparison between the experimental results and the reference data. The task becomes more difficult if we deal with multi-phase samples. To solve this problem, Szymanski et al. [34] proposed an approach, in which the augmentation of computed XRD patterns is used to make prediction of phase more correctly. The augmentation procedure was designed to sample possible experimental artifacts including peak shift associated with cell strain, peak broadening related to small domain size and peak intensity variation caused by texture. The neural network consisted of input layer (one-dimensional vector $\vec{x} \in R^{1 \times 14501}$ associated with the intensity of the XRD spectrum as a function of 2θ), six convolution layers (with pooling, flattening was applied after last layer) and fully connected neural network with two hidden layers. As result CNN gives probability of corresponding phases. The branching algorithm implemented in the model allows one to use it for multi-phase identification.

To train CNN model the dataset of Mo-B structures is collected. It includes the structures of molybdenum borides (45), boron oxides (3), boron (1) and molybdenum (1) phases and also structures of molybdenum carbide (4) because carbide electrodes are used in the experimental part of this work and there is an opportunity to obtain some amounts of carbides. The data set combined the structures from Material-Project resource as well as structures obtained from USPEX predictions [21–23]. As a result, the data used to train a model consisted of 54 unique structures. Distribution of selected structure by boron content and point symmetry over across the dataset is presented in Fig. 2. One can note that the largest number of structures belongs to higher molybdenum borides with the boron atom fraction of 0.8, see left panel in Fig. 2. This is associated with different models of MoB_{5-x} ($x = 0 \dots 0.8$) used for simulations. Simulated diffraction patterns of predicted structures with respect to experimental diffraction patterns are shown in Fig. S4.

3. Results and discussion

As mentioned in previous works of the authors [19,35–37], one of the main features of the vacuum-free electric arc method is the synthesis of different materials by arc discharge plasma under ambient conditions at normal pressure. Obtaining non-oxide materials under such conditions is possible due to intensive generation of carbon monoxide and carbon dioxide gases during the arcing, which form an autonomous self-shielded gas medium. To confirm this thesis for the first time in the field of synthesis of molybdenum borides by vacuum-free DC arc discharge method, the composition of the gas medium in the reaction zone, namely, in the cavity of the external graphite crucible, was analyzed using a gas analyzer. As can be seen from Fig. 1b, during DC arcing in air, the oxygen concentration decreases from the normal value (~21 vol%) to almost zero (~0.5 vol%), while at the same time there is a significant release of carbon monoxide and carbon dioxide gases, the maximum concentration of which reaches ~16.5 vol% and ~30.9 vol%, respectively. This creates the shielding effect of the reaction zone. At the end of arcing the oxygen increases to the initial concentration, i.e. the reaction zone is filled with air. It is worth noting that a decrease in the oxygen concentration in the reaction zone during the arcing leads to an increase in the concentration of carbon monoxide CO, in turn, the concentration of carbon dioxide CO_2 decreases. The reverse process is observed after stop arcing: the concentration of CO decreases, and the concentration of CO_2 increases. This effect can be caused by a deficiency of O_2 in the reaction zone, resulting in the formation of a CO compound instead of CO_2 . After stop arcing the reaction zone is filled with air, resulting in the oxidation of the carbon monoxide CO to carbon dioxide CO_2 . According to the literature [38], in the beginning of the arc discharge process, all oxygen in air were reacted immediately with carbon atoms due to high

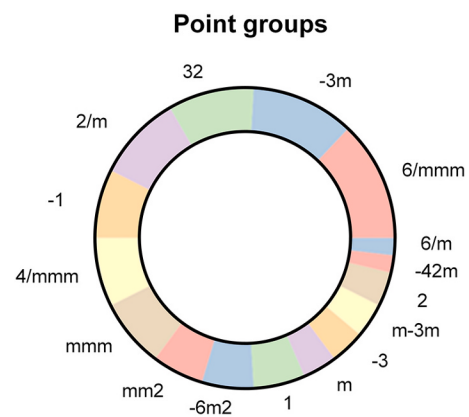
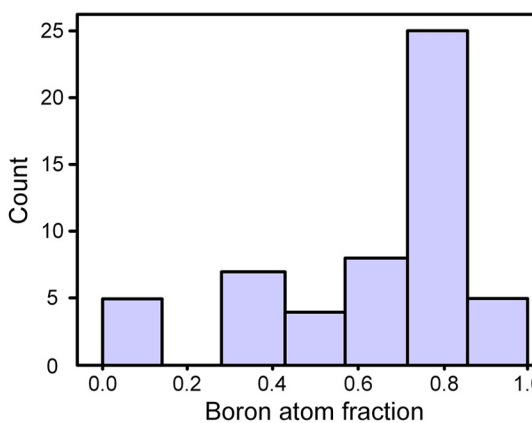


Fig. 2. Distribution of data on crystal structures used for training of CNN model for identification of XRD reflections.

temperature of arc plasma, forming CO_2 . Then, carbon atoms were reacted with the formed CO_2 to CO . However, according to the work [39], as a result of arc discharge process atmospheric oxygen reacts with carbon first forming carbon monoxide CO , which is then oxidized to carbon dioxide CO_2 . Regardless of the above-mentioned contradictions in the literature data, the authors of this study suggest that both reactions take place simultaneously in the reaction zone, depending on the point at which the measurements are taken. It is worth noting that the autonomous gas environment consisting of CO and CO_2 gases persists for some time after the end of arcing, which promotes the formation of crystalline phases of molybdenum borides.

The temperature field distribution taken with an infrared camera during the vacuum-free electric arc synthesis of molybdenum borides is shown in Fig. 1c. The plasma exposure time in the experiment is 40 s. The IR thermograms show a temperature gradient along both the external and inner crucibles. However, the gradient decreases as the plasma exposure time increases. According to Ref. [40], the synthesis of molybdenum borides requires temperatures of 1200–1500 °C. According to the obtained IR thermograms, at a plasma exposure time of 40 s, the average temperature of the outer wall of the small inner crucible is ~1338 °C, and the maximum temperature exceeds 1550 °C. Therefore, the realized conditions are sufficient for the synthesis of molybdenum borides by vacuum-free electric arc method. In addition, the flow-through in the external crucible made for this experiment, obviously, increases the thermal energy losses in the system, so the obtained data are somewhat underestimated relative to the real synthesis. The accuracy of temperature measurement using an infrared camera depends on

factors such as the emissivity and reflectivity of the object surface, the ambient temperature and the distance to the measuring object [41], which may also introduce measurement errors.

Three series of experiments in the molybdenum-boron system are prepared at different current, plasma exposure time, and precursors Mo:B ratios. X-ray phase analysis is performed for each experiment and interpreted using CNN [34]. The trained model allows us to determine not only qualitative, but also quantitative phase composition by sequential comparison of phase diffraction patterns and using branching algorithm described above. The results of phases identification by CNN are shown in Table S1, Fig. S4-S5 in the Supporting Information. At the same time, Table S3 presents quantitative data on the identified crystalline phases and their correlations with cards from the PDF4+database.

The first series of experiments aims to study the influence of the current controlled by the power supply on the phase composition of the obtained powder. The experiments are carried out with currents of 50, 100, 150, and 200 A with a fixed plasma exposure time of 40 s. In this case, the molybdenum to boron ratio Mo:B = 1:3 at. is chosen to obtain the well-known MoB_2 modification. The overestimation of the boron content is due to the peculiarities of vacuum-free electric arc synthesis: boron can vaporize and oxidize and then vaporize as part of the oxide before the formation of a protective gas medium during the initiation and combustion of the arc discharge in the cavity of the external graphite crucible. In addition, many papers on the synthesis of metal borides by various methods overestimate the amount of boron due to its possible losses during the synthesis. According to the XRD data (Fig. 3),

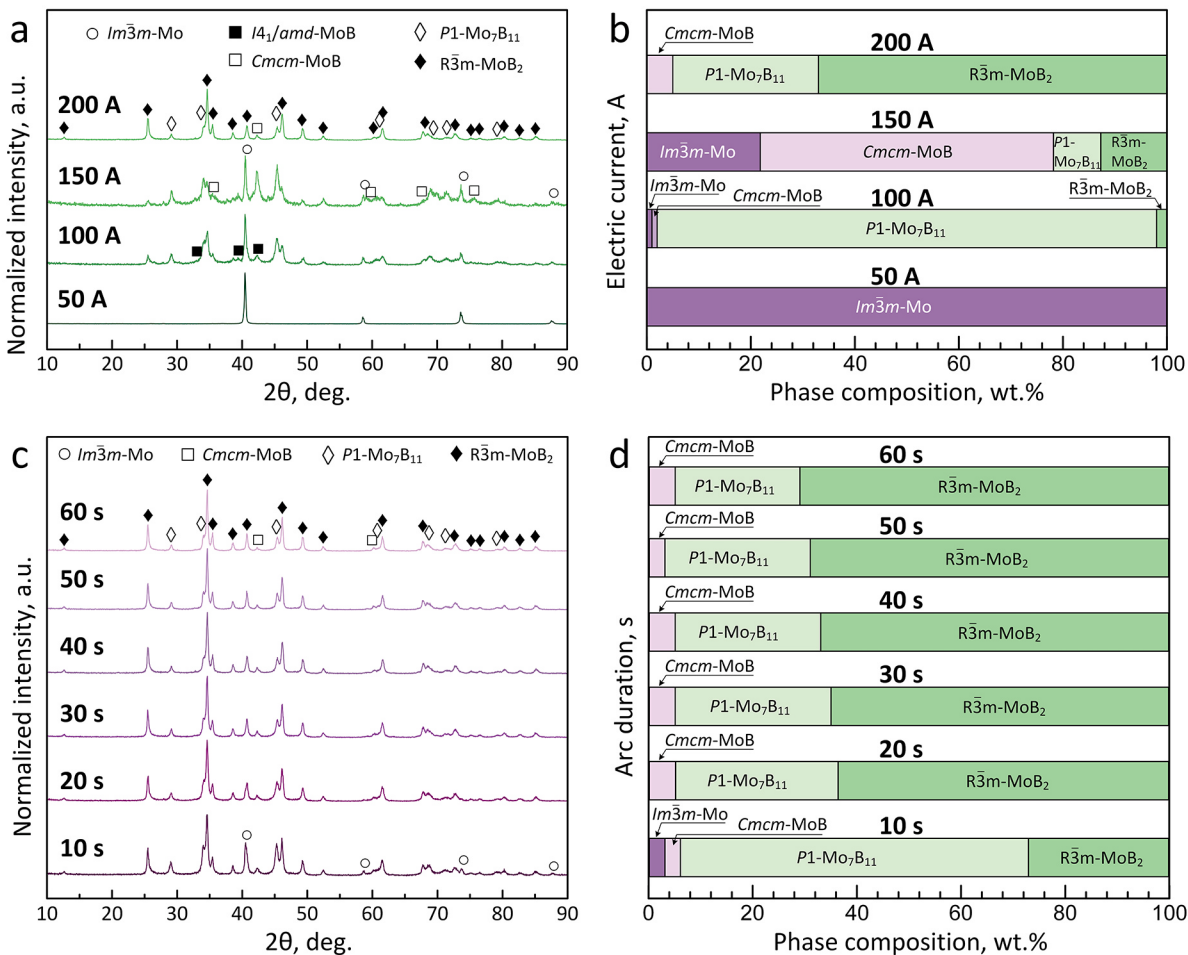


Fig. 3. XRD patterns and quantitative XRD analysis of synthesized samples with different electric current (a, b) and with different time of plasma treatment (c, d).

at a current of 50 A, the X-ray diffraction patterns show reflections corresponding exclusively to the phase of the initial molybdenum $I\bar{m}\bar{3}m$ -Mo (Mo, PDF4+ Card No. 01-077-8340). This indicates that the amount of energy supplied is insufficient to trigger the reaction between the initial components ($W = 28.85$ kJ, Table S2). In Fig. 3a, it can be observed that the diffraction maxima of molybdenum are preserved when the current is increased up to and including $I = 150$ A. The interaction of initial molybdenum and boron to form the molybdenum boride phases $I4_1/and$ -MoB (α -MoB, PDF4+ Card No. 00-051-0940), $P1$ -Mo₇B₁₁ and $R\bar{3}m$ -MoB₂ (PDF4+ Card No. 89-3786) are recorded in the sample obtained at $I = 100$ A. Further increase of the current up to 150 A leads to the formation of the $Cmcm$ -MoB (β -MoB, PDF4+ Card No. 6-644) crystalline phase. The clearest X-ray diffraction pattern with the maximum degree of crystallinity is observed in the sample obtained at $I = 200$ A. In this case, the main maximum belongs to the $R\bar{3}m$ -MoB₂ phase, in addition there are small intensity diffraction maxima corresponding to the $P1$ -Mo₇B₁₁ and $Cmcm$ -MoB phases. In this regard, the supply current of 200 A is chosen for further experiments.

The XRD patterns of the samples synthesized at 10, 20, 30, 40, 50 and 60 s plasma exposure time while keeping the other parameters constant (current 200 A, Mo:B = 1:3 at.) are shown in Fig. 3c. According to the

results obtained, it can be seen that $I\bar{m}\bar{3}m$ -Mo, $Cmcm$ -MoB, $P1$ -Mo₇B₁₁, $R\bar{3}m$ -MoB₂ phases are present in the as-synthesized samples. It should be noted that $P1$ -Mo₇B₁₁ can be considered as a defective version of $P6_3/mmc$ -MoB₂. The XRD patterns of $P1$ -Mo₇B₁₁ and $P6_3/mmc$ -MoB₂ are similar, but due to the lower symmetry $P1$ -Mo₇B₁₁ fits the experimental data better. A similar situation of prediction of different defective versions of more symmetric prototypes was observed in the tungsten-boron system [9]. In this case, with increasing exposure time from 10 s to 40 s, the intensity of diffraction maxima of $I\bar{m}\bar{3}m$ -Mo, $Cmcm$ -MoB, $P1$ -Mo₇B₁₁ phases decreases, while for $R\bar{3}m$ -MoB₂ – increases. The X-ray diffraction patterns of the samples obtained at $t = 40, 50, 60$ s do not differ significantly, therefore it is decided to use $t = 40$ s to ensure energy efficiency in subsequent experiments.

Fig. 4a shows the XRD patterns of the samples synthesized with changing the ratio of initial components of molybdenum and boron, with increasing the proportion of boron from 1 to 25 at., at the parameters determined by the previous experiments ($t = 40$ s, $I = 200$ A). The series are conducted to obtain all known phases in the molybdenum–boron system by the vacuum-free electric arc method.

The X-ray diffraction pattern of the sample synthesized at Mo:B = 1:1 at. shows the presence of diffraction maxima corresponding to Mo

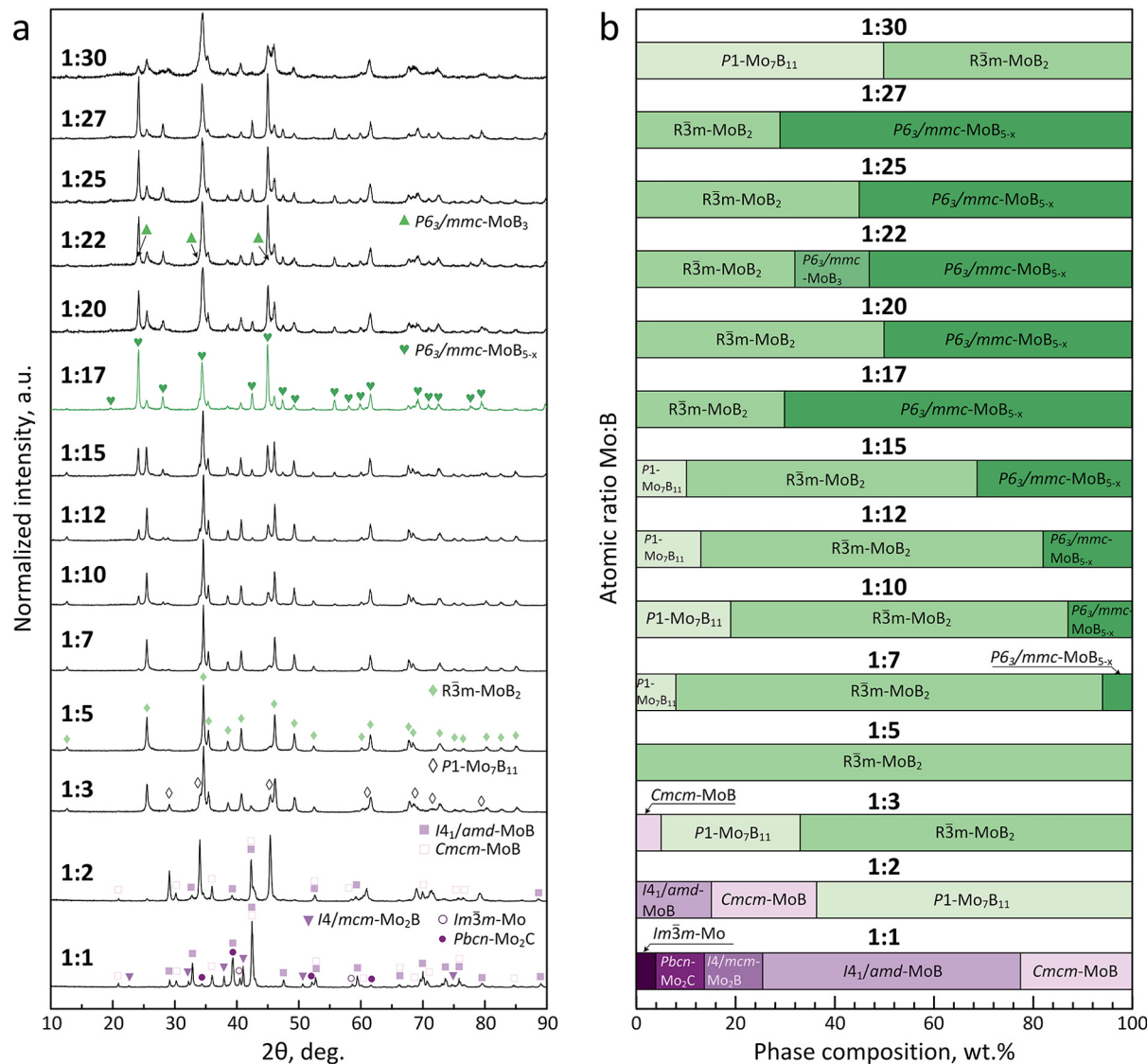


Fig. 4. XRD patterns (a) and quantitative XRD analysis (b) of synthesized samples with different Mo:B at. ratio.

($\bar{Im}\bar{3}m$ -Mo), Mo_2B ($I4/mcm$ - Mo_2B , ICDD Card No. 04-001-0962), α - MoB ($J4_1/AMD$ - MoB), β - MoB ($Cmcm$ - MoB), and Mo_2C ($Pbcn$ - Mo_2C , PDF4+ Card No. 04-016-3695) phases. There is a boron deficiency in the system, which in the first seconds of arcing, before the formation of the self-shielded gas medium consisting of gases CO and CO_2 , can react with oxygen in the air to form boron oxide B_2O_3 , respectively, boron deficiency appears in the system. In this regard, molybdenum in the system becomes more abundant relative to boron, and phases Mo, Mo_2C and Mo_2B are formed. Similar results are described in Ref. [14]. When increasing the boron content in 2 times ($Mo:B = 1:2$) the initial molybdenum is completely converted to molybdenum borides α - MoB , β - MoB , $MoB_{1.57}$, with the most intense reflections belonging to the $MoB_{1.57}$ phase, formed by the lack of boron in the system. The X-ray diffraction pattern of the sample obtained at the ratio $Mo:B = 1:5$ at. (200 A, 40 s) completely coincides with the reference one for the crystalline phase MoB_2 ; no diffraction maxima belonging to other phases were found. The obtained result suggests that it is necessary to overestimate the boron fraction in the initial mixture by at least 1.5–2.0 times for the synthesis of a certain phase of molybdenum boride by vacuum-free electric arc method. The deliberate overestimation of the proportion of boron in the initial mixture during the synthesis of metal borides is known and has been described in other studies (for example, in the works [19,42–44]. With increasing boron fraction from 7 to 27 at., the corresponding X-ray diffraction patterns of the samples (Fig. 4) identify diffraction maxima located at $2\theta = 24.2, 28.2, 34.5, 45.0^\circ$, belonging to the calculated phase of molybdenum boride MoB_{5-x} ($P6_3/mmc$) with crystal planes indices $(\bar{1}23)$, (006) , (300) , $(\bar{3}06)$, respectively. In these samples, $MoB_{1.57}$, MoB_2 and MoB_3 phases are also present. The formation of several phases of molybdenum borides simultaneously can be attributed to the presence of a temperature field gradient in the reaction zone (Fig. 1, c): regions with high temperatures of the order of 1500 °C are formed, in which the formation of the highest molybdenum boride begins, taking into account the loss of boron at the initial stage of formation of the autonomous gas medium, and as one moves away from the zone with the highest temperatures, a boron deficit arises and $MoB_{1.57}$, MoB_2 , MoB_3 borides are formed. According to the quantitative analysis, the proportion of MoB_{5-x} crystalline phase increases from 6 to 71 wt% when the boron fraction increases from 7 to 27 at. Increasing the amount of boron to 1:30 does not result in a larger amount of the higher molybdenum boride phase. In this regard, the optimal parameters of synthesis samples with ~70 wt% of higher molybdenum boride MoB_{5-x} are current strength of 200 A, arc exposure time of 40 s, molybdenum to boron atomic ratio of 1:17, because the higher boride is maximum with a minimum of boron excess in the initial mixture.

It should be noticed that $Mo:B$ atom ratio makes the biggest contribution to chemical composition of the system, obtaining after experiment. For example, by increasing the proportion of boron atoms, it is possible to synthesize a mixture rich in higher borides (Fig. 5).

Further, the morphology and elemental composition of samples obtained at $Mo:B = 1:1; 1:2; 1:5; 1:15; 1:25$ at. are studied by scanning electron microscopy. SEM images of the micron fraction, shown in Fig. 6, are obtained in low vacuum mode by backscattered electron (BSE) and secondary electron (SE) detectors. Several types of objects can be distinguished from the obtained images. The first type includes agglomerated particle clusters (Fig. 6f), the sizes of such clusters are on average from 10 μm to 550 μm . It is found that the frequency of agglomerates appearance on SEM images increases with increasing boron fraction in samples. Also based on brightness with increasing boron fraction in the initial mixture, the samples are represented by darker particles with a larger number of agglomerates (Fig. 6a-e). The particles, which are part of agglomerates and occur separately, are characterized by a flake-like shape of the order of 0.3–3.0 μm in size (type 2, Fig. 6g). According to energy dispersive analysis, their composition contains the following elements: Mo (28.5 ± 8.5 at.%), B (66.6 ± 9.5 at.%), O ($3.9 \pm$

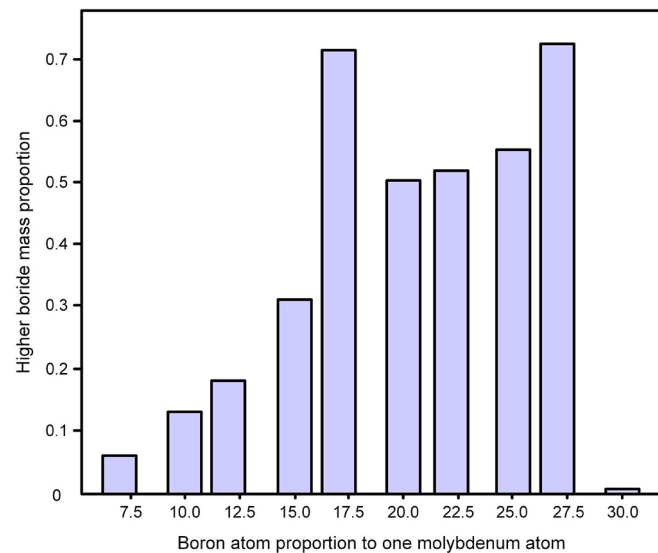


Fig. 5. Increasing the higher boride fraction depending on initial $Mo:B$ atom ratio.

1.2 at.%). The third type is represented by spherical particles with diameters from 2 to 25 μm (Fig. 6h), probably formed by the vapor-liquid-crystal (VLS) mechanism. In addition, some of these particles may be characterized by cracks and fractures. The elemental composition of spherical particles is characterized by Mo (26.3 ± 5.9 at. %), B (70.0 ± 3.1 at. %), and O (6.0 ± 1.1 at. %) atoms. The fourth type includes shapeless particles embedded in an amorphous boron matrix (B ~ 89.5 ± 5.6 at.%) (Fig. 6i-j). This type of objects is found in samples with high boron content. In terms of elemental composition, the shapeless particles are mainly composed of boron (80.2 ± 7.8 at. %) and molybdenum (20.2 ± 5.7 at. %). The formation of particles containing molybdenum and boron atoms is also confirmed by the elemental mapping shown in Fig. S6.

The nanoscale fraction of the obtained samples is studied by transmission electron microscopy. Fig. 7 shows typical TEM results. According to the light-field overview image (Fig. 7a), the samples contain single particles and particles immersed in the matrix, probably boron. The particle size distribution varies from ~50 nm to ~500 nm. The SAED pattern (Fig. 7b) from the region highlighted in Fig. 7a contains a set of reflections, the comparison of the interplanar distances of which with the reference ones shows the correspondence to $R\bar{3}m$ - MoB_2 , $P6_3/mmc$ - MoB_{5-x} phases (Table 1). The presence of boron oxide B_2O_3 ($d_{200} = 4.36$ Å) is explained by the high boron content in the samples and its surface oxidation due to storage and transportation of the samples in air. According to energy dispersive analysis (Fig. 7c), the particles contain atoms of molybdenum, boron and some impurities (nitrogen, oxygen, carbon). The interplanar distance determined from the HRTEM image (Fig. 7d) is $d \sim 0.26$ and $d \sim 0.27$ nm correlates with the reference $d_{300} \sim 0.26$ nm and $d_{\bar{3}12} \sim 0.28$ nm for the $P6_3/mmc$ - MoB_{5-x} phase considering the possible error. The angle between the crystallographic planes (300) and ($\bar{3}12$) is ~133°, which indicates the hexagonal structure of the sample. Thus, TEM results confirm the successful synthesis of molybdenum borides, including the highest molybdenum boride.

Then, to study the mechanical properties of molybdenum borides, ceramic samples based on synthesized powders were prepared by spark plasma sintering. XRD results of sintered samples are presented in Fig. 8 and Fig. S7 in the Supporting Information. The presence of phase transformations as a result of the sintering is observed. In the sample $Mo:B = 1:1$ during the SPS due to the created temperature conditions of initial molybdenum reacts with carbon, as a result, the proportion of molybdenum carbide phase increases (Table S4, Fig. S8 in the

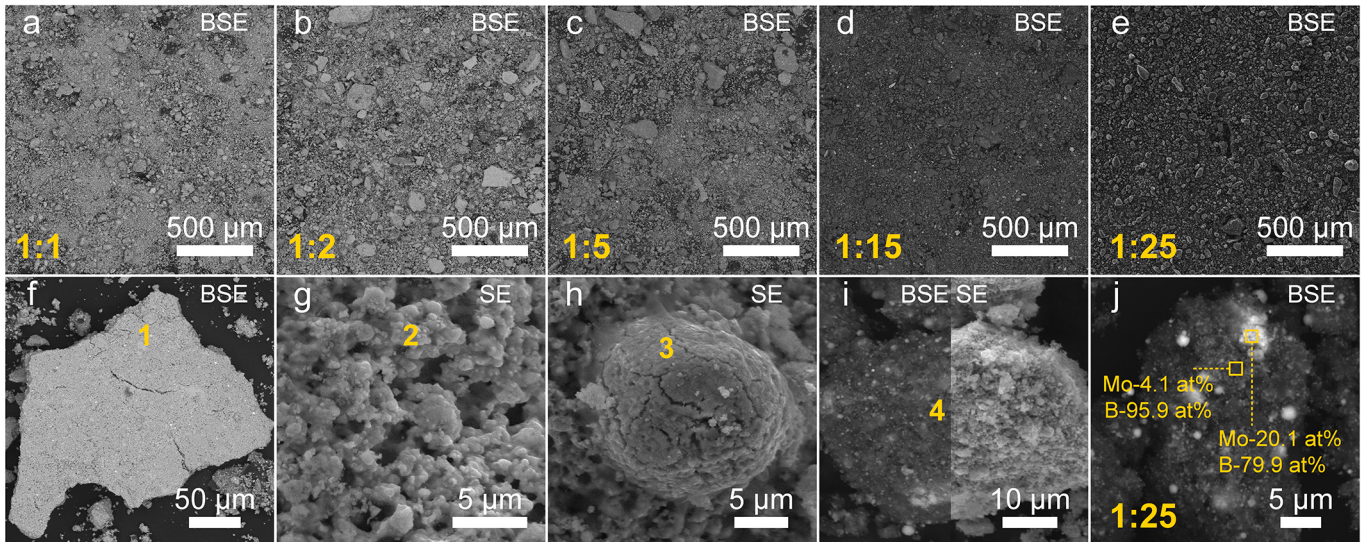


Fig. 6. SEM-images of synthesized samples with Mo:B = 1:1 (a), 1:3 (b), 1:5 (c), 1:15 (d), 1:25 (e) and different morphological types (f-j).

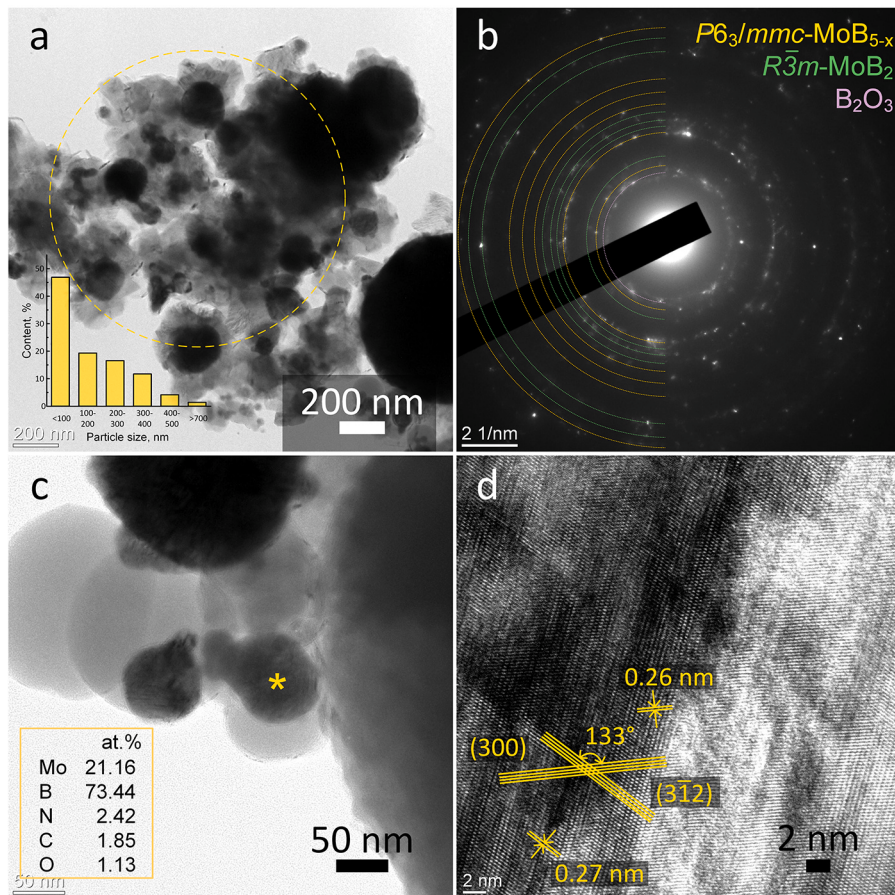


Fig. 7. Bright-field TEM image with particle size distribution inset (a); SAED pattern from selected area (b); bright-field TEM image with EDX inset (c); HRTEM image (d).

Supporting Information). The Mo:B = 1:5 sample after sintering consists exclusively of the $MoB_{1.57}$ molybdenum boride phase, according to XRD (Table S4, Fig. S9 in the Supporting Information). There is a phase of higher molybdenum boride MoB_{5-x} in the composition of Mo:B = 1:15 and 1:25 samples before sintering, but the X-ray diffraction pattern of sintered ceramics shows the presence of two phases of molybdenum

boride – MoB_2 and $MoB_{1.57}$. Thus, the results of XRD of samples before and after SPS indicate phase transitions directed towards the reduction of boron amount in molybdenum borides.

One can note that temperature treatment of powder of higher molybdenum boride leads to reduction of boron content and transition to diboride structure, or to defected versions of diboride structures. This

Table 1

Comparison of reference interplanar distance with observed interplanar distance of the SAED pattern.

d, Å (observed, Fig. 7b)	d _{hkl} , Å (reference)	Crystal phase
3.84 ± 0.01	d ₂₀₃ = 3.67	P6 ₃ /mmc-MoB _{5-x}
3.49 ± 0.07	d ₀₀₆ = 3.48	R̄3m-MoB ₂
2.67 ± 0.02	d ₂₂₀ = 2.62	P6 ₃ /mmc-MoB _{5-x}
2.49 ± 0.03	d ₁₋₁₂ = 2.54	R̄3m-MoB ₂
2.38 ± 0.02	d ₁₀₄ = 2.34	R̄3m-MoB ₂
2.23 ± 0.02	d ₁₁₅ = 2.22	R̄3m-MoB ₂
2.10 ± 0.02	d ₀₄₃ = 2.11	P6 ₃ /mmc-MoB _{5-x}
1.92 ± 0.03	d ₂₄₆ = 2.00	P6 ₃ /mmc-MoB _{5-x}
1.76 ± 0.03	d ₄₂₃ = 1.65	P6 ₃ /mmc-MoB _{5-x}
1.51 ± 0.01	d ₁₁₀ = 1.51	R̄3m-MoB ₂
1.40 ± 0.01	d ₁₁₆ = 1.38	R̄3m-MoB ₂
1.33 ± 0.01	d ₂₂₁₂ = 1.34	P6 ₃ /mmc-MoB _{5-x}

can be related to the calculated evolution of the stability convex hull diagram of M–B phases with temperature, see Fig. S10 in the Supporting Information. Crystal structures for calculations were taken both from this work and from Ref. [8]. As one can note, during the experimental synthesis, we do not fall into the exact MoB_{5-x} composition, the other borides with less boron content may be formed. Evolution of convex hull with temperature shows quite steep slope of the curve between MoB₅ and MoB₂ structures, meaning a slip in composition or subsequent heating will lead to breakdown and the formation of other borides.

Fig. 9 shows the comparison of the microstructure of the sintered powder samples. Images in the phase-contrast mode together with elemental analysis allowed to establish the interface boundaries in the samples. According to EDX elemental composition includes: 52.2 ± 3.2 at.% of Mo and 47.8 ± 3.2 at.% of B which close to phase MoB determined early by XRD of Mo:B = 1:1 sample (Fig. 9a); the following ratio of Mo:B (61.2 ± 2.9 at.% of Mo and 38.8 ± 2.9 at.% of B) is close to phase MoB_{1.57} (Fig. 9b); 34.1 ± 2.0 at.% of Mo and 65.9 ± 2.0 at.% of B for phase MoB₂ (Fig. 9c-e). The relative density of sintered samples determined by the Archimedes method decreases from 7.39 g/cm³ to 2.87 g/cm³ with increasing amount of boron. As can be seen from SEM images, the samples contain multiple pores, as well as samples 1:5–1:25 have excess boron. Therefore, the density of each sample is lower than the theoretical density (Table S5 in the Supporting Information).

The velocity of longitudinal and shear ultrasonic waves were measured and used to calculate the elastic moduli (longitudinal and shear moduli) (Table S5 in the Supporting Information). It is worth noting that for sample 1:25 it was not possible to measure the elastic moduli due to the poor sintering of the sample because of the significant

presence of free amorphous boron in the composition. For the ceramic samples based on molybdenum boride, Vickers hardness values were measured using a dynamic ultra-micro hardness tester with a Berkovich indenter. Table 2 summarizes the obtained mechanical characterization data in comparison with literature data. As can be seen, the highest average (for 10 points) hardness (37.83 ± 9.42 GPa) is characterized by the sample Mo:B = 1:5. At the same time, in some points the hardness value reaches about 50 and 60 GPa. As can be seen, most of the works on the study of mechanical characteristics are calculated. Among the experimental works, bulk ceramic samples were obtained mainly by HPHT method and their hardness was measured. As can be seen, the measured elastic moduli of the obtained samples are lower than similar calculated values in the literature, which is due to the low density of the samples. At the same time, the obtained ceramic samples based on molybdenum borides are characterized by increased hardness values.

4. Conclusion

The synthesis and characterization of molybdenum-boron powders synthesized by using the vacuum-free direct-current arc discharge method is performed. It is found that phase composition of the synthesis product can be tuned by adjusting the set-up parameters, namely the power supply current, the arcing time and the ratio of raw powder material. The application of a convolution neural network approach for analysis of X-ray diffraction data allows the quantitative identification of the molybdenum boride phases in the obtained powders. The following molybdenum borides are obtained: I4/mcm-Mo₂B, I4₁/amd-MoB (α -MoB), Cmcm-MoB (β -MoB), P1-Mo₇B₁₁, R̄3m-MoB₂, P6₃/mmc-MoB₃, P6₃/mmc-MoB_{5-x}. It is found that at a current of 200 A, arc duration time of 40 s and Mo:B = 1:5 at. it is possible to synthesize almost pure powder of R̄3m-MoB₂. In addition, the corresponding X-ray diffraction patterns of samples obtained at Mo:B ratios from 1:7 to 1:27 at. identify diffraction maxima located at $2\theta = 24.2, 28.2, 34.5, 45.0^\circ$, belonging to the higher molybdenum boride MoB_{5-x}. At the same time, as the atomic fraction of boron in the composition of the raw Mo:B mixture increases from 7 to 27, the fraction of the crystalline MoB_{5-x} increases from 6 to 71 wt%. For the ceramic samples based on higher molybdenum borides, the Vickers hardness are measured, showing that ceramic sample with Mo:B = 1:5 possesses the highest average hardness among other synthesized borides of 37.83 ± 9.42 GPa. The results obtained in this work make it possible to extend the scope of the vacuum-free electric arc method for the synthesis of various borides, including higher borides.

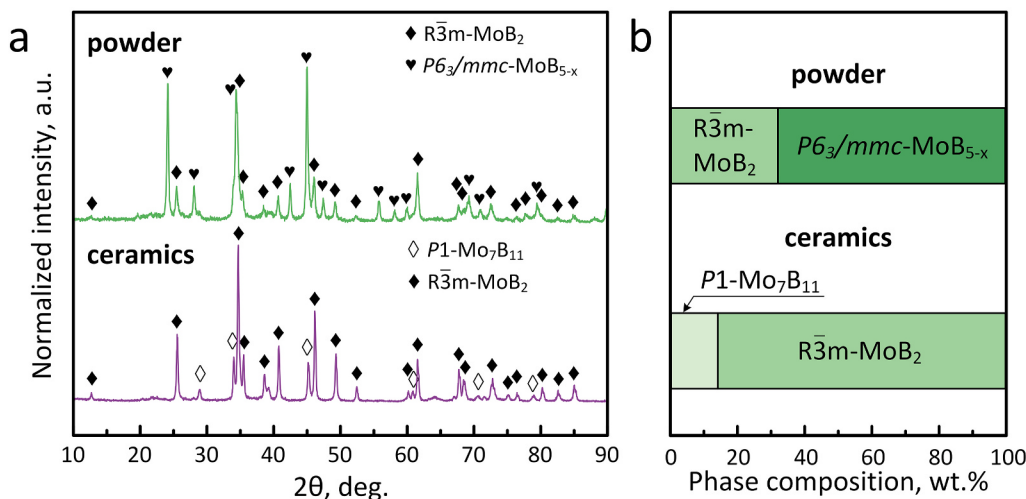


Fig. 8. XRD patterns (a) and quantitative XRD analysis (b) of samples Mo:B = 1:25 before and after SPS.

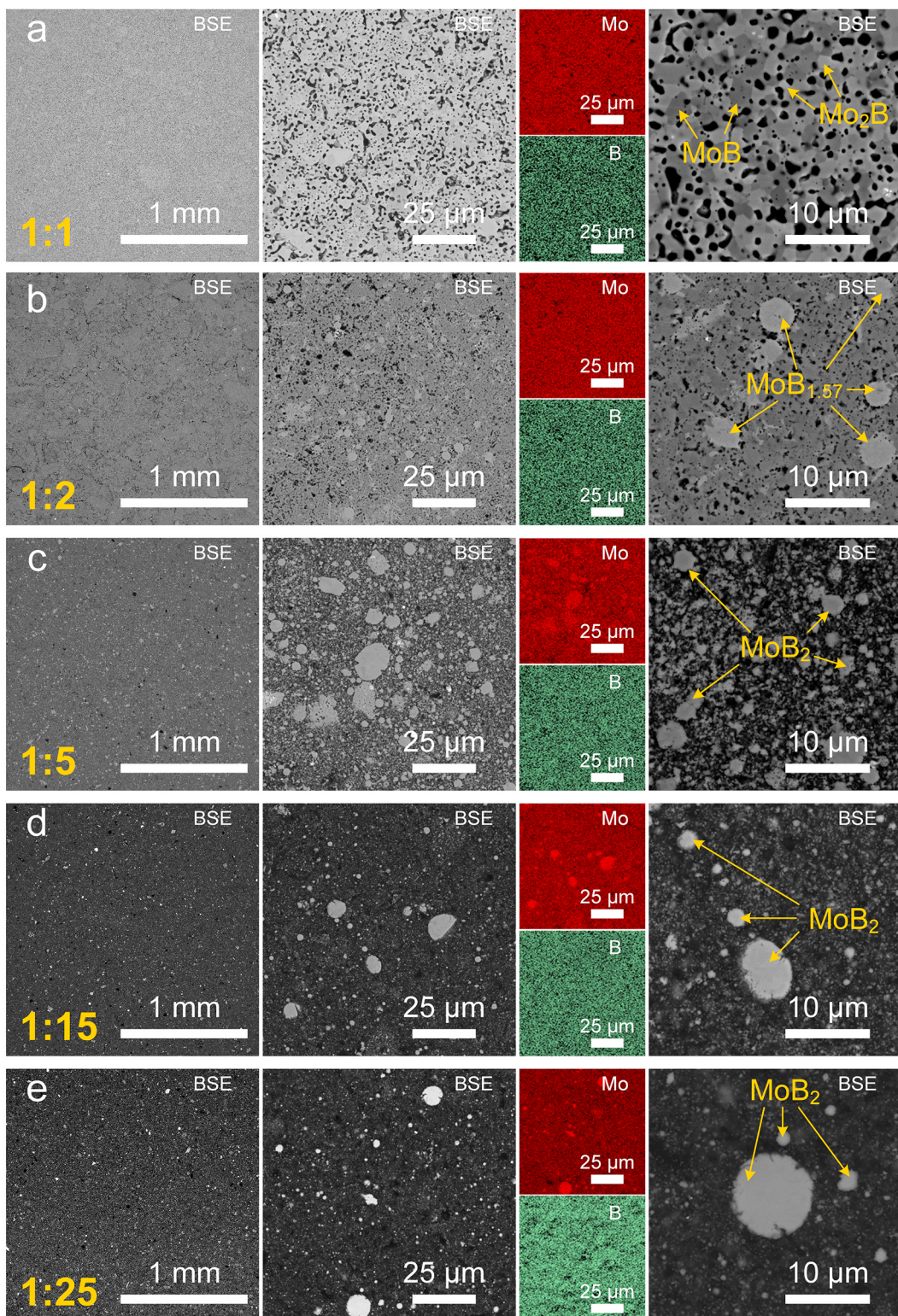


Fig. 9. SEM images and elemental mapping of Mo-B ceramics: 1:1 (a), 1:2 (b), 1:5 (c), 1:15 (d), 1:25 (e).

CRediT authorship contribution statement

Yuliya Vassilyeva: Writing – original draft, Project administration, Investigation, Funding acquisition, Conceptualization. **Yulia Neklyia:** Visualization, Validation, Formal analysis. **Mikhail Lukanov:** Software, Formal analysis, Data curation. **Alexander Kvashnin:** Writing – original

draft, Software, Methodology. **Alexander Pak:** Writing – review & editing, Resources, Methodology.

Declaration of competing interest

The authors declare that they have no known competing financial

Table 2

Comparison of mechanical characteristics of the obtained samples in the “molybdenum–boron” system with literature data.

Material	Method	E, GPa	G, GPa	HV, GPa (load)	Reference
Mo:B = 1:1 (Mo_2C , Mo_2B , $\alpha\text{-MoB}$)	Vacuum-free arc synthesis	287	119	25.46 ± 3.59 (100 mN)	this work
Mo:B = 1:2 ($\alpha\text{-MoB}$, $\beta\text{-MoB}$, $\text{MoB}_{1.57}$)	Vacuum-free arc synthesis	313	133	29.90 ± 2.65 (100 mN)	this work
Mo:B = 1:5 (MoB_2)	Vacuum-free arc synthesis	254	109	37.83 ± 9.42 (100 mN)	this work
Mo:B = 1:15 ($\text{MoB}_{1.57}$, MoB_2)	Vacuum-free arc synthesis	216	98	30.53 ± 3.96 (100 mN)	this work
Mo:B = 1:25 ($\text{MoB}_{1.57}$, MoB_2)	Vacuum-free arc synthesis	–	–	17.49 ± 5.93 (100 mN)	this work
Mo_2B 140- Mo_2B	theoretical	389	151	18.9	[45]
87- Mo_2B	theoretical	398	155	14.5	[46]
$\alpha\text{-MoB}$	theoretical	391	152	14.2	[46]
$\alpha\text{-MoB}$ (nano- polycrystal)	theoretical	519	210	21.3	[45]
$\alpha\text{-MoB}$ (nano- polycrystal)	theoretical	–	205	18.4	[47]
141- MoB	HPHT	–	–	24.1 (0.98 N) 19.5 (1.96 N)18.4 (2.94 N)18.4 (4.9 N)	[47]
63- MoB	theoretical	507	205	23.8	[46]
$I_4/\text{amd-}\text{MoB}$	theoretical	468	487	20.2	[46]
$Cmc\bar{m}\text{-}\text{MoB}$	theoretical	500	203	24.523.2	[8]
$\beta\text{-MoB}$	theoretical	478	193	22.121.9	[8]
$\beta\text{-MoB}$ (nano- polycrystal)	theoretical	496	199	21.3	[45]
$\beta\text{-MoB}$ (nano- polycrystal)	theoretical	–	194	12.2	[47]
141- MoB	HPHT	–	–	20.9 (1 N) 16.9 (2 N)14.1 (3 N)12.2 (5 N)	[47]
MoB	heating in H_2	–	–	23.0	[48]
$\beta\text{-MoB}$	heating in H_2	–	–	24.5	[48]
MoB_2	theoretical	569	238	24.4	[45]
$hP3\text{-}\text{MoB}_2$	theoretical	429	169	16.4	[49]
$hR18\text{-}\text{MoB}_2$	theoretical	572	239	33.1	[49]
191- MoB_2	theoretical	419	164	15.6	[46]
194- MoB_2	theoretical	533	220	28.7	[46]
$\alpha\text{-MoB}_2$	theoretical	463	186	15.9	[50]
$\alpha\text{-MoB}_2$	HPHT	–	–	15.2	[50]
$\beta\text{-MoB}_2$	theoretical	522	216	21.2	[50]
$\beta\text{-MoB}_2$	HPHT	–	–	22.0	[50]
$R\bar{3}m\text{-}\text{MoB}_2$	theoretical	548	230	32.430.3	[8]
MoB_2	aluminium-flux technique	–	–	24.2	[51]
MoB_4	HPHT	535	223	38–39	[18]
$M_{0.757}\text{B}_3$	HPHT	486	206	33.9–39.3	[18]
MoB_5	theoretical	554	232	22.8	[45]
$hR21\text{-}\text{MoB}_5$	theoretical	304	114	7.0	[49]
MoB_3	theoretical	526	222	31.8	[45]
$hP16\text{-}\text{MoB}_3$	theoretical	554	237	37.3	[49]
$R\bar{3}m\text{-}\text{MoB}_3$	theoretical	522	222	34.933.2	[8]
$P6_3/mmc\text{-}\text{MoB}_3$	theoretical	527	225	35.533.8	[8]
MoB_4	theoretical	206	210	24.8	[45]
$hP20\text{-}\text{MoB}_4$	theoretical	306	116	8.2	[49]
$Pmmn\text{-}\text{MoB}_5$	theoretical	538	232	38.637.3	[8]

interests or personal relationships that could have appeared to influence the work reported in this paper.

Acknowledgement

The research was funded by the grant No 23-79-01145 from Russian Science Foundation.

Appendix A. Supplementary data

Supplementary data to this article can be found online at <https://doi.org/10.1016/j.tsep.2025.104134>

Data availability

Data will be made available on request.

References

- [1] E.S. Penev, S. Bhowmick, A. Sadrzadeh, B.I. Yakobson, Polymorphism of two-dimensional boron, *Nano Lett.* 12 (2012) 2441–2445, <https://doi.org/10.1021/nl3004754>.
- [2] X. Wang, P. Fan, Y. Xie, L. Zhang, J. Jiang, P. Huang, J. Zhao, Ruthenium-doped molybdenum boride for electrocatalytic hydrogen evolution, *Fuel* 388 (2025) 134550, <https://doi.org/10.1016/j.fuel.2025.134550>.
- [3] L. Zhang, X. Wang, H. Ye, Y. Xie, J. Jiang, Y. Guo, J. Zhao, Rare-earth lanthanum doped molybdenum borides for electrocatalytic hydrogen evolution reaction, *J. Alloy. Compd.* 1022 (2025) 179876, <https://doi.org/10.1016/j.jallcom.2025.179876>.
- [4] X. Wang, G. Tai, Z. Wu, T. Hu, R. Wang, Ultrathin molybdenum boride films for highly efficient catalysis of the hydrogen evolution reaction, *J. Mater. Chem. A* 5 (2017) 23471–23475, <https://doi.org/10.1039/c7ta08597d>.
- [5] H.E. Çamurlu, Preparation of single phase molybdenum boride, *J. Alloy. Compd.* 509 (2011) 5431–5436, <https://doi.org/10.1016/j.jallcom.2011.02.083>.
- [6] A.W. Weimer, in: *Carbide, Nitride and Boride Materials Synthesis and Processing*, Springer Science & Business Media, 1997, <https://doi.org/10.1007/978-94-009-0071-4>.
- [7] Y. Wang, H. Zhang, S. Jiao, K.C. Chou, G.H. Zhang, A facile pathway to prepare molybdenum boride powder from molybdenum and boron carbide, *J. Am. Ceram. Soc.* 103 (2020) 2399–2406, <https://doi.org/10.1111/jace.16984>.
- [8] D.V. Rybkovskiy, A.G. Kvashnin, Y.A. Kvashnina, A.R. Oganov, Structure, stability, and mechanical properties of boron-rich Mo-B phases: A computational study, *J. Phys. Chem. Lett.* 11 (2020) 2393–2401, <https://doi.org/10.1021/acs.jpclett.0c00242>.
- [9] A.G. Kvashnin, H.A. Zakaryan, C. Zhao, Y. Duan, Y.A. Kvashnina, C. Xie, H. Dong, A.R. Oganov, New tungsten borides, their stability and outstanding mechanical properties, *J. Phys. Chem. Lett.* 9 (2018) 3470–3477, <https://doi.org/10.1021/acs.jpclett.8b01262>.
- [10] K. Kudaka, K. Iizumi, T. Sasaki, S. Okada, Mechanochemical synthesis of MoB_2 and Mo_2B_5 , *J. Alloys Compounds* 315 (2001) 104–107, [https://doi.org/10.1016/S0925-8388\(00\)01082-3](https://doi.org/10.1016/S0925-8388(00)01082-3).
- [11] S.A. Kuznetsov, E.V. Rebrov, M.J.M. Mies, M.H.J.M. de Croon, J.C. Schouten, Synthesis of protective Mo-Si-B coatings in molten salts and their oxidation behavior in an air-water mixture, *Surf. Coat. Technol.* 201 (2006) 971–978, <https://doi.org/10.1016/j.surcoat.2006.01.003>.
- [12] C.L. Yeh, W.S. Hsu, Preparation of molybdenum borides by combustion synthesis involving solid-phase displacement reactions, *J. Alloy. Compd.* 457 (2008) 191–197, <https://doi.org/10.1016/j.jallcom.2007.03.024>.
- [13] Y. Li, Y. Fan, Y. Chen, A novel route to nanosized molybdenum boride and carbide and/or metallic molybdenum by thermo-synthesis method from MoO_3 , KBH_4 , and CCl_4 , *J. Solid State Chem.* 170 (2003) 135–141, [https://doi.org/10.1016/S0022-4596\(02\)00044-0](https://doi.org/10.1016/S0022-4596(02)00044-0).
- [14] H. Park, A. Encinas, J.P. Scheifers, Y. Zhang, B.P.T. Fokwa, Boron-dependency of molybdenum boride electrocatalysts for the hydrogen evolution reaction, *Angewandte Chemie - International Edition* 56 (2017) 5575–5578, <https://doi.org/10.1002/anie.201611756>.
- [15] F. Zhao, Q. Tao, C. You, M. Ye, L. Li, Y. Han, S. Dong, X. Wang, T. Cui, P. Zhu, Enhanced hardness in tungsten-substituted molybdenum diboride solid solutions by local symmetry reduction, *Mater. Chem. Phys.* 251 (2020) 123188, <https://doi.org/10.1016/j.matchemphys.2020.123188>.
- [16] P.R. Jothi, K. Yubuta, B.P.T. Fokwa, A simple, general synthetic route toward nanoscale transition metal borides, *Adv. Mater.* 30 (2018) 1704181, <https://doi.org/10.1002/adma.201704181>.
- [17] Y. Chen, G. Yu, W. Chen, Y. Liu, G.D. Li, P. Zhu, Zou X. Highly active, nonprecious electrocatalyst comprising borophene subunits for the hydrogen evolution reaction, *J. Am. Chem. Soc.* 139 (2017) 12370–12373, <https://doi.org/10.1021/jacs.7b06337>.
- [18] H. Tang, X. Gao, J. Zhang, B. Gao, W. Zhou, B. Yan, X. Li, Q. Zhang, S. Peng, D. Huang, Boron-rich molybdenum boride with unusual short-range vacancy ordering, anisotropic hardness, and superconductivity, *Chem. Mater.* 32 (2019) 459–467, <https://doi.org/10.1021/acs.chemmater.9b04052>.
- [19] A.Y. Pak, D.V. Rybkovskiy, Y.Z. Vassilyeva, E.N. Kolobova, A.V. Filimonenko, A. G. Kvashnin, Efficient Synthesis of $\text{WB}_{5-x}\text{-}\text{WB}_2$ Powders with Selectivity for WB_{5-x} Content, *Inorg. Chem.* 61 (2022) 6773–6784, <https://doi.org/10.1021/acs.inorgchem.1c03880>.
- [20] A.R. Oganov, Y. Ma, A.O. Lyakhov, M. Valle, C. Gatti, Evolutionary crystal structure prediction as a method for the discovery of minerals and materials, *Rev. Mineral. Geochem.* 71 (2010) 271–298, <https://doi.org/10.2138/rmg.2010.71.13>.
- [21] A.R. Oganov, C.W. Glass, Crystal structure prediction using ab initio evolutionary techniques: Principles and applications, *J. Chem. Phys.* 124 (2006), <https://doi.org/10.1063/1.2210932>.

- [22] A.R. Oganov, A.O. Lyakhov, M. Valle, How evolutionary crystal structure prediction works-and why, *Acc. Chem. Res.* 44 (2011) 227–237, <https://doi.org/10.1021/ar1001318>.
- [23] A.O. Lyakhov, A.R. Oganov, H.T. Stokes, Q. Zhu, New developments in evolutionary structure prediction algorithm USPEX, *Comput. Phys. Commun.* 184 (2013) 1172–1182, <https://doi.org/10.1016/j.cpc.2012.12.009>.
- [24] P. Hohenberg, W. Kohn, Inhomogeneous electron gas, *Phys. Rev.* 136 (1964) B864, <https://doi.org/10.1103/PhysRev.136.B864>.
- [25] W. Kohn, L.J. Sham, Self-consistent equations including exchange and correlation effects, *Phys. Rev.* 140 (1965) A1133, <https://doi.org/10.1103/PhysRev.140.A1133>.
- [26] J.P. Perdew, K. Burke, M. Ernzerhof, Generalized gradient approximation made simple, *Phys. Rev. Lett.* 77 (1996) 3865–3868, <https://doi.org/10.1103/PhysRevLett.77.3865>.
- [27] P.E. Blöchl, Projector augmented-wave method, *Phys. Rev. B* 50 (1994) 17953, <https://doi.org/10.1103/PhysRevB.50.17953>.
- [28] D. Joubert, From ultrasoft pseudopotentials to the projector augmented-wave method, *Phys. Rev. B - Condensed Matter Mater. Phys.* 59 (1999) 1758–1775, <https://doi.org/10.1103/PhysRevB.59.1758>.
- [29] G. Kresse, J. Furthmüller, Efficient iterative schemes for ab initio total-energy calculations using a plane-wave basis set, *Phys. Rev. B - Condens. Matter Mater. Phys.* 54 (1996) 11169–11186, <https://doi.org/10.1103/PhysRevB.54.11169>.
- [30] G. Kresse, J. Hafner, Ab initio molecular-dynamics simulation of the liquid-metalamorphous- semiconductor transition in germanium, *Phys. Rev. B* 49 (1994) 14251–14269, <https://doi.org/10.1103/PhysRevB.49.14251>.
- [31] G. Kresse, J. Hafner, Ab initio molecular dynamics for liquid metals, *Phys. Rev. B* 47 (1993) 558, <https://doi.org/10.1103/PhysRevB.47.558>.
- [32] M. Methfessel, A.T. Paxton, High-precision sampling for Brillouin-zone integration in metals, *Phys. Rev. B* 40 (1989) 3616–3621, <https://doi.org/10.1103/PhysRevB.40.3616>.
- [33] G. Kern, G. Kresse, J. Hafner, Ab initio calculation of the lattice dynamics and phase diagram of boron nitride, *Phys. Rev. B - Condens. Matter Mater. Phys.* 59 (1999) 8551–8559, <https://doi.org/10.1103/PhysRevB.59.8551>.
- [34] N.J. Szymanski, C.J. Bartel, Y. Zeng, Q. Tu, G. Ceder, Probabilistic deep learning approach to automate the interpretation of multi-phase diffraction spectra, *Chem. Mater.* 33 (2021) 4204–4215, <https://doi.org/10.1021/acs.chemmater.1c01071>.
- [35] A.Y. Pak, I.I. Shanenkov, G.Y. Mamontov, A.I. Kokorina, Vacuumless synthesis of tungsten carbide in a self-shielding atmospheric plasma of DC arc discharge, *Int. J. Refract. Met. Hard Mater.* 93 (2020) 105343, <https://doi.org/10.1016/j.ijrmhm.2020.105343>.
- [36] Y.Z. Vassilyeva, K.B. Larionov, S.D. Afonnikova, P.V. Povalyaev, U.S. Komkina, Y. A. Neklyu, I.V. Mishakov, A.Y. Pak, Synthesis of Mo₂C-based material in DC arc discharge plasma under ambient air conditions, *Mater. Chem. Phys.* 314 (2024) 128805, <https://doi.org/10.1016/j.matchemphys.2023.128805>.
- [37] A.Y. Pak, P.S. Grinchuk, A.A. Gumovskaya, Y.Z. Vassilyeva, Synthesis of transition metal carbides and high-entropy carbide TiZrNbHfTaC₅ in self-shielding DC arc discharge plasma, *Ceram. Int.* 48 (2022) 3818–3825, <https://doi.org/10.1016/j.ceramint.2021.10.165>.
- [38] Y. Su, H. Wei, T. Li, H. Geng, Y. Zhang, Low-cost synthesis of single-walled carbon nanotubes by low-pressure air arc discharge, *Mater. Res. Bull.* 50 (2014) 23–25, <https://doi.org/10.1016/j.materresbull.2013.10.013>.
- [39] N. Li, Z. Wang, K. Zhao, Z. Shi, Z. Gu, S. Xu, Synthesis of single-wall carbon nanohorns by arc-discharge in air and their formation mechanism, *Carbon* 48 (2010) 1580–1585, <https://doi.org/10.1016/j.carbon.2009.12.055>.
- [40] X.H. Yang, Y. Wang, G.H. Zhang, K.C. Chou, Size-controlled preparations of tungsten and molybdenum borides in calcium or aluminum melt, *Ceram. Int.* 49 (2023) 5357–5370, <https://doi.org/10.1016/j.ceramint.2022.10.059>.
- [41] Y.C. Zhang, Z. Wang, X. Fu, F. Yan, T. Kong, An experimental method for improving temperature measurement accuracy of infrared thermal imager, *Infrared Phys. Technol.* 102 (2019) 103020, <https://doi.org/10.1016/j.infrared.2019.103020>.
- [42] G. Sun, X. Zhao, L. Chen, Y. Fu, W. Zhao, M. Ye, P. Zhu, Synthesis of Ni-B compounds by high-pressure and high-temperature method, *ACS Omega* 8 (2023) 9265–9274, <https://doi.org/10.1021/acsomega.2c07523>.
- [43] C. Gu, Y. Liang, X. Zhou, J. Chen, D. Ma, J. Qin, S. Wang, Crystal structures and formation mechanisms of boron-rich tungsten borides, *Phys. Rev. B* 104 (2021) 014110, <https://doi.org/10.1103/PhysRevB.104.014110>.
- [44] C.L. Yeh, J.Z. Lin, H.J. Wang, Formation of chromium borides by combustion synthesis involving borothermic and aluminothermic reduction of Cr₂O₃, *Ceram. Int.* 38 (2012) 5691–5697, <https://doi.org/10.1016/j.ceramint.2012.04.013>.
- [45] M. Zhang, H. Wang, H. Wang, T. Cui, Y. Ma, Structural modifications and mechanical properties of molybdenum borides from first principles, *J. Phys. Chem. C* 114 (2010) 6722–6725, <https://doi.org/10.1021/jp100225c>.
- [46] H. Zhu, L. Shi, S. Li, Y. Duan, W. Xia, Y. Wang, Influence of uniaxial strains on the mechanical properties of transition metal borides X₂B, XB and XB₂ (X = Cr Mo, W), *Phys. B: Condens. Matter* 550 (2018) 100–111, <https://doi.org/10.1016/j.physb.2018.09.008>.
- [47] Q. Tao, Y. Chen, M. Lian, C. Xu, L. Li, X. Feng, X. Wang, T. Cui, W. Zheng, P. Zhu, Modulating hardness in molybdenum monoborides by adjusting an array of boron zigzag chains, *Chem. Mater.* 31 (2019) 200–206, <https://doi.org/10.1021/acs.chemmater.8b04154>.
- [48] R. Steinitz, I. Binder, D. Moskowitz, System molybdenum-boron and some properties of the molybdenum-borides, *JOM* 4 (1952) 983–987, <https://doi.org/10.1007/BF03397758>.
- [49] Y. Liang, X. Yuan, Z. Fu, Y. Li, Z. Zhong, An unusual variation of stability and hardness in molybdenum borides, *Appl. Phys. Lett.* 101 (2012), <https://doi.org/10.1063/1.4764547>.
- [50] Q. Tao, X. Zhao, Y. Chen, J. Li, Q. Li, Y. Ma, J. Li, T. Cui, P. Zhu, X. Wang, Enhanced Vickers hardness by quasi-3D boron network in MoB₂, *RSC Adv.* 3 (2013) 18317–18322, <https://doi.org/10.1039/C3RA42741B>.
- [51] S. Okada, T. Atoda, I. Higashi, Y. Takahashi, Preparation of single crystals of MoB₂ by the aluminium-flux technique and some of their properties, *J. Mater. Sci.* 22 (1987) 2993–2999, <https://doi.org/10.1007/BF01086503>.